Research Article | Vol. 28, No. 9 / 27 April 2020 / Optics Express 12977

Optics EXPRESS

Far-field Talbot waveforms generated by acousto-optic frequency shifting loops

JUAN CLEMENT,[1] HUGUES GUILLET DE CHATELLUS,[2] AND CARLOS R. FERNÁNDEZ-POUSA[1,*]

[1] *Engineering Research Center (I3E), Dep. of Communications Engineering, Univ. Miguel Hernández, 03202 Elche, Spain*
[2] *Univ. Grenoble Alpes, CNRS, LIPhy, 38000 Grenoble, France*
[*] *c.pousa@umh.es*

Abstract: We report on the description of the optical fields generated by acousto-optic Frequency-Shifting Loops (FSL) in the temporal Fraunhofer domain when the loop is operated in the vicinity of integer or fractional Talbot conditions. Using self-heterodyne detection, we experimentally demonstrate the equivalence of the Talbot phases generated at fractional conditions with the Gauss perfect phase sequences, and identify deviations from the standard frequency-to-time mapping description of the far field. In particular, we show the existence of ripples in the pulse intensity, of unavoidable pulse-to-pulse interference in the pulse train, of small oscillations, of the order of hundreds of MHz, in the expected linear pulse chirp, and the capture of the phase at the pulse's trailing edge by the adjacent pulse. Using asymptotic analysis, we construct a field model that accounts for these features, which are due to corrections to the frequency-to-time mapped field created by the sharp spectral edge of the FSL spectrum, in analogy to diffraction. Practical design consequences for signal generation and processing systems based on FSL are discussed.

1. Introduction

There exists a continuous demand of multipurpose optical sources amenable to integration in a diversity of photonic systems. Among them, cw injection-seeded frequency shifted lasers and loops have recently emerged as compact and versatile subsystems providing technical alternatives in a variety of application fields. Essentially, they consist of an amplified loop cavity, fed by a coherent carrier, where a frequency shifting element is inserted so that the injected wave is repeatedly frequency shifted at each pass through the loop. They can be operated either below or at the laser threshold in loop or laser conditions, respectively, generating optical frequency combs (OFC) with a spectral separation determined by the shifting element. Extensively studied in free space configurations (see [1,2] and references therein), this concept has also been explored in fiber loops and lasers incorporating both electro-optic [3–7] and acousto-optic [8–18] shifting devices compatible with standard C-band telecom technology.

Fiber-based frequency shifting loops (FSL) using acousto-optic frequency shifters (AOFS) typically provide OFC with spectral separations in the range of several tens of MHz, a figure that can be decreased to the kHz range by inserting two AOFS with frequency shifts of opposite signs. Their spectral widths can reach tens of GHz, resulting in combs comprising up to about one thousand lines with demonstrated use in high resolution spectroscopy [8–10]. In the temporal domain, an ample field of applications is enabled by the loops' ability to generate pulse trains with widths in the ns range and with tunable lowest-order dispersion at different seed wavelengths. This fact has permitted the implementation, over the same basic platform, of photonic signal processors based on optical real-time Fourier [11] and fractional Fourier [12] transformations, the electrical generation of chirped [13] and arbitrary [14] waveforms, Doppler velocimeters [15], laser range finders [16] and spectral shapers [17]. On the other hand, frequency-shifted laser's main application has been the implementation of fractional temporal Talbot effect for the

#384515 https://doi.org/10.1364/OE.384515
Journal © 2020 Received 11 Dec 2019; revised 23 Jan 2020; accepted 24 Jan 2020; published 16 Apr 2020

Optics EXPRESS

generation of high repetition rate pulse trains [18]. A brief account of these developments has recently been published [19], and general references of the theory of Talbot effect are [20–23].

In the case of loops, the induced dispersion permits the generation of highly dispersed pulse trains lying in the temporal far field of Fraunhofer region, which may also show the increase of repetition rate characteristic of fractional Talbot effect. It is precisely in this context, the analysis of these optical waveforms, where the present investigation is inscribed. In particular, two aspects of these waves have been targeted. On the one hand, pulse trains obtained by stretching fractional Talbot fields inherit its main properties and, in particular, their relative phases. As is well-known [23], pulses in a fractionally-imagined Talbot pulse train show different phases arranged cyclically within the train, with a periodicity equal to the factor describing the increase in the repetition rate of the intensity. In FSL, dispersion allows for the stretching of these pulses, thus enabling the direct measurement of the Talbot phases using self-heterodyne detection, a measurement that has only been carried out in the angular implementation of the Talbot effect [24]. On the other hand, the OFC generated by FSL presents, by construction, a spectral edge, *i.e.*, a step-like discontinuity in its spectrum. This particularity is specific of these optical generators and is not shown, for instance, by mode-locked lasers, where the gain profile is usually quadratic and thus results in pulses with smooth, gaussian-like spectra. Neither can this edge be implemented by an optical filter, since it would violate causality, nor through single-sideband electro-optic modulation [25], as the induced spectral edges always show residual sidebands. The analysis of the field with an exact spectral edge seems not to have been previously addressed in the literature, and will be object of particular attention here.

The relevance of the two targeted features encompasses both theoretical and practical aspects of acousto-optic FSL. The phases arising in Talbot effect are known to be arranged in the so-called perfect Gauss sequences [26], their cyclic correlation properties being responsible for instance, of the increase in pulse repetition rate [23], the coherent sum of waves enabling spatial [27] and temporal [28] Talbot array illuminators, the reversible transformation of coherent spectra leading to cloaking systems [29], or a variety of photonic signal processing techniques [30]. The existence of a spectral edge, in turn, allows for the recovery of the complete, complex optical electrical field with self-heterodyne detection, thus avoiding the use of I/Q receivers [16], and the analysis of the optical phase in the far field provides performance parameters and design rules in the generation of broadband chirped waveforms [13]. This second aspect deserves a specific theoretical analysis since, although the theory of Talbot effect is well understood [20–23,26,31–33] the FSL temporal waveforms in the temporal Fraunhofer region present peculiar features analogous to the one-dimensional diffraction of straight edges which have not been analyzed before.

The objective of this paper in thus twofold. On the one hand, to present a direct measurement of the phases generated by Talbot effect in the temporal domain and, on the other, to provide a both theoretical and experimental analysis of the chirped fields generated by FSL in the temporal far field, highlighting the temporal effects that arise from the propagation of waves with spectral edges in analogy with one-dimensional diffraction, and which are here described for the first time to the best of our knowledge.

This paper is organized as follows. In Section 2 we describe the basic layout of an acousto-optic FSL and the fields generated at and out of integer or fractional temporal Talbot conditions. Section 3 is devoted to the analysis of the temporal Fraunhofer field of waves with a spectral edge by means of the asymptotic expansion of the field in inverse powers of the spectral Fresnel number. Similar expansions have been derived in the analysis of a variety of radiation problems [34], and are extended here to the description of the frequency chirp. The detailed computations are presented separately in the Appendix. Section 4 describes the experimental results and the comparison of the theoretical far field model with the experimental data. Finally, our conclusions are presented in Section 5.

Optics EXPRESS

2. Optical fields generated by FSL

An unidirectional cw injection-seeded acousto-optic FSL, schematically shown in Fig. 1(a), consists of a cw laser that feeds a fiber loop, composed of an optical isolator that forces unidirectional propagation, an EDFA as a gain medium, an optical tunable bandpass filter (TBPF), and an acousto-optic frequency shifter (AOFS). The role of the AOFS is to shift the frequency of the incoming light by a fixed amount f_s so that the loop generates a number of recirculating frequencies in the form of an optical frequency comb with spectral separation f_s. A large number of comb lines, hundreds or even more than one thousand of frequencies, can be sustained thanks to the presence of the EDFA. The TBPF defines the total bandwidth of the optical comb that may reach several tens of GHz, and rejects part of the amplified spontaneous emission (ASE) from the EDFA which would otherwise be reinjected in the amplifier.

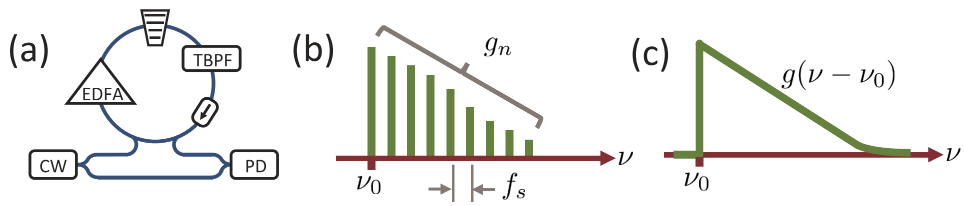

Fig. 1. (b) Scheme of a FSL: CW, continuous-wave laser; EDFA, erbium-doped fiber amplifier; TBPF, tunable bandpass filter; PD, high-bandwidth photodiode. The direct path from CW to PD is used for the heterodyne field measurements. (b) Scheme of the single-sided optical frequency comb of the FSL: ν, optical frequency; ν_0, seed frequency; f_s, shifting frequency; g_n, spectral amplitudes in logarithmic scale. (c) Scheme of the spectrum of the transform-limited pulse $g(f) = g(\nu - \nu_0)$.

Let us denote by $\mathcal{E}(t) = E_{in} \exp(j2\pi\nu_0 t)$ the electric field describing the cw injection, with ν_0 the seed frequency and E_{in} the injected amplitude. Assuming that the frequency shift f_s imparted by the AOFS is positive, the output field is a one-sided comb of optical harmonics at frequencies $\nu_n = \nu_0 + nf_s$, with $n = 0, 1, \ldots$ [1,2], as is schematically represented in Fig. 1(b). Let us denote by τ_c the loop's round trip time and by g_n the spectral amplitude at ν_n. Then, a FSL frequency comb composed of, say, N frequencies can be assumed coherent provided that the coherence time of the cw injection laser exceeds $N\tau_c$. The wave's spectral width is thus $\Delta\nu = (N-1)f_s \simeq Nf_s$, and the output envelope is a coherent sum of optical harmonics $n = 0, \ldots, N-1$ each with a phase factor resulting from the accumulated propagation delay associated to the multiple pass through the loop at increasing shifted frequencies. The resulting envelope can be written as [1,2]:

$$E_{FSL}(t) = \sum_{n=0}^{N-1} g_n e^{-j\pi f_s \tau_c n(n+1) - j2\pi n\nu_0\tau_c} e^{j2\pi n f_s t} \tag{1}$$

Note that in this derivation it is implicitly assumed the absence of dispersive effects in the propagation through the loop, and so the spectral phases are proportional to the constant, and thus wavelength-independent, round-trip time τ_c. The accumulated spectral phase of the n-th harmonic is, however, quadratic in the mode index n, and therefore the combination of frequency shifting and recirculation induces lowest-order dispersion in the periodic output field. The spectral amplitudes in Eq. (1) are given by $g_n = E_{in}(\eta a)^n$, with η the single-pass round-trip transmission coefficient and a the amplitude gain imparted by the EDFA. This approximation, which assumes loss and gain independent of wavelength, results in an overall exponentially decreasing spectral amplitude. The actual magnitudes of g_n depend on the relative values of this exponential decay and the bandwidth imposed by the TBPF: with $\eta a \lesssim 1$ the exponential spectral decay is slow, and the actual spectral width is determined by the TBPF rejection band. As the

Optics EXPRESS

value of ηa is decreased, the decay becomes purely exponential and the TBPF role is to solely reject ASE. Examples of these two regimes can be observed, for instance, in [16]. In either case, we can assume that the spectral decay of the amplitudes g_n is smooth, so that the number N of spectral lines in Eq. (1) is to be interpreted as the number of significant observable lines in a given experimental situation.

2.1. Fields at Talbot conditions

We begin our analysis of Eq. (1) with its second term in the spectral phase factor, $\exp(-j2\pi n\nu_0\tau_c)$, which describes a global delay $\tau_d = \nu_0\tau_c/f_s$ linear in the seed optical frequency ν_0. This delay induces a wavelength-to-time mapping that is exploited in signal processors and generators when the FSL is fed with different wavelengths [11]. In our case, the FSL is fed by a single seed wavelength, so we neglect this global delay in what follows. The FSL pulse trains are thus controlled by the product $f_s\tau_c$ in the first term of the spectral phase factor, and can be described using the theory of temporal Talbot effect [23]. When the product $f_s\tau_c$ equals an integer number p, requirement that is referred to as the integer temporal Talbot condition, the spectral lines in Eq. (1) are in phase and the FSL envelope is a periodic train of transform-limited pulses with period $T = 1/f_s$, which can be presented as:

$$E_{FSL}(t) = \sum_{m=-\infty}^{+\infty} E_0(t - mT) \tag{2}$$

Note that the product $n(n + 1)$ is always even and therefore there is no half-period shift for odd values of p as in the standard description of the effect [23].

To describe the individual pulses $E_0(t)$, we denote by $g(\nu - \nu_0)$ the comb's spectral amplitude measured from the seed frequency ν_0, as shown in Fig. 1(c). This spectral amplitude consists of a spectral edge, $g(\nu - \nu_0) = 0$ for $\nu<\nu_0$, followed by a smooth decay interpolating the spectral harmonics, $g(nf_s) = g_n$. The existence of this smooth decay is justified by the relatively low bandwidth of the spectral comb and the broadband character of the the optical elements comprising the loop. Alternatively, and using $f = \nu - \nu_0$, spectrum $g(f)$ can be defined through the Fourier transform of the transform-limited basic pulse in Eq. (2),

$$E_0(t) = \int_0^{\infty} df\, g(f)e^{j2\pi ft} \tag{3}$$

The validity of this description deserves some comments. The introduction of function $g(f)$ through Eq. (3) depends on the decomposition of the pulse train presented in Eq. (2) in individual and temporally separated pulses $E_0(t)$. This implicit assumption is not very stringent in the case, for instance, of mode-locked lasers, where the typical gaussian-like decay of their pulses justifies the standard hypotheses of negligible pulse-to-pulse interference or high extinction ratio. In the case of the transform-limited pulses generated by FSL, the presence of a spectral edge induces a slower asymptotic pulse decay of the form $\sim g(0)/(2\pi jt)$, which can be inferred from Eq. (3) by integration by parts [35]. This fact may invalidate the description of the pulse train $E_{FSL}(t)$ in terms of isolated entities if this slow decay leads to severe pulse-to-pulse interference. Function $g(f)$ in Eq. (3) is thus only intended to be sensitive for the most favourable situation, the integer Talbot condition described above, where pulses are separated by a period of typically ~10 ns. To provide a practical estimate of this approximation, the typical FWHM pulse width of a 20-GHz OFC is about 50 ps, which seems sufficient to be confident with Eqs. (2) and (3). In either case, we stress that the pulse train is experimentally built up and mathematically described by the discrete set of spectral amplitudes g_n in Eq. (1), and so any other single-pulse spectral amplitude, say $\tilde{g}(f)$, such that $\tilde{g}(nf_s) = g_n$ for $n \geq 0$ and zero for $n<0$ could have been used to describe the train. The choice in Eq. (3) is the simplest compatible with the experimental evidences, namely the expected smooth character of $g(f)$ and the absence of optical frequencies below the seed frequency, and permits a direct asymptotic analysis as will be shown below.

Fractional Talbot effect [23], in turn, corresponds to fractional values of the above mentioned product, $f_s\tau_c = p/q$, with p and q coprime integers. In this case, the linear term in n in the first phase term in Eq. (1) represents again a global delay $\tau_c/2 = pT/(2q)$. The FSL envelope is [26,33]:

$$E_{FSL}(t) = \frac{e^{j\xi_0}}{\sqrt{q}} \sum_{m=-\infty}^{+\infty} e^{j\pi \frac{s}{q} m^2} E_0(t - mT/q - \epsilon_{pq}T/2) \tag{4}$$

where ϵ_{pq} denotes the parity of the product pq, *i.e.* $\epsilon_{pq} = 1$ for pq odd and zero for pq even, and where we have omitted the $\tau_c/2$ delay. Hence, the train consists of a series of transform-limited pulses mutually separated by a fraction T/q of the original period. Each of these pulses is multiplied by a quadratic phase factor which depends on an integer s whose actual value is a function of both p and q. Integer s has the opposite parity to that of q, so that $\exp(j\pi \frac{s}{q} n^2) = \exp(j\pi \frac{s}{q}(n+q)^2)$ and therefore the period in Eq. (4) is $T = 1/f_s$, as it is determined by the shifting frequency. Factor $\exp(j\xi_0)$ is a constant phase that only depends on integers p and q, and which will therefore be omitted in the rest of our analysis.

When the temporal width of the transform-limited basic pulse $E_0(t)$ is lower than T/q, the intensity of the field described by Eq. (4) is composed of q equalized transform-limited pulses per period, thus showing a q-fold increase in the pulse repetition rate with respect to the field at integer Talbot conditions in Eq. (2). However, loops allow for the generation of a wider class of optical waveforms out of these Talbot conditions, as is analyzed in the following subsection.

2.2. Fields out of Talbot conditions

To analyze this situation we write, near an arbitrary fractional Talbot condition,

$$f_s\tau_c = \frac{p}{q} + \delta f_s \tau_c \tag{5}$$

for a certain frequency mismatch δf_s. According to Eq. (1), this mismatch induces an additional quadratic phase factor to each of the frequencies in the comb. As a consequence, the train of integer or fractional Talbot transform-limited pulses undergoes an additional group velocity dispersion (GVD) $\phi = \tau_c \delta f_s/(2\pi f_s^2)$ that originates trains of chirped pulses [13]. This induced GVD attains large values even for small frequency mismatches: for typical values $f_s = 100$ MHz, $\tau_c = 10$ ns, and $\delta f_s = 50$ kHz, we get $\phi \sim 10^4$ ps^2/rad, corresponding to the dispersion of ~500 km of standard single-mode fiber in the C band. The resulting pulse train has the same form as in Eq. (2) or Eq. (4), but now the envelope of its basic pulse is given by:

$$E(t) = \int_0^{\infty} df\, g(f) e^{-j2\pi^2 \phi f^2} e^{j2\pi f t} = \frac{e^{-j\mathrm{sign}(\phi)\pi/4}}{\sqrt{2\pi|\phi|}} \int_{-\infty}^{\infty} dt'\, E_0(t') e^{j(t-t')^2/2\phi} \tag{6}$$

In the second part of the equation we have used the temporal Fresnel propagator to express the dispersed envelope as a convolution integral. Note that $E(t,-\phi) = E^*(-t,\phi)$, and so we will restrict our analysis to positive GVD, $\phi>0$ or $\delta f_s>0$, without loss of generality.

Let us denote by $\Delta\nu$ the spectral width of $g(f)$. Then, the temporal extent of the transform-limited pulse $E_0(t)$ can be estimated as $\Delta t_0 = 1/\Delta\nu$. Using these scales, we define the temporal and spectral Fresnel numbers as $\alpha_t = \Delta t_0^2/(2\pi\phi)$ and $\alpha_\nu = 2\pi\phi\Delta\nu^2$, respectively. These Fresnel numbers are inverse to each other, a fact that simply reflects the duality between the temporal and spectral representations of the field in Eq. (6).

To justify these definitions, recall that the (diffractive) Fresnel number is given by $N_F = a^2/(\lambda_0 z)$, with a the aperture's dimension, λ_0 the wavelength, and z the propagation distance. From the last part of Eq. (6), the temporal width Δt_0 is equivalent to the aperture a, whereas ratio $1/(\lambda_0 z)$

Optics EXPRESS

coincides with the phase prefactor in the Fresnel diffraction integral divided by π, as in our definition of α_t. Because of the same type of identifications, the spectral Fresnel number follows after completing the phase in the first part of Eq. (6) to a perfect square, thus producing again a Fresnel propagator, and then noticing that $\Delta\nu$ plays here the role of a spectral aperture.

The temporal Fresnel number near an integer or fractional Talbot condition can attain very small values: using the previously mentioned figures and a typical spectral width $\Delta\nu = 20$ GHz we obtain $\alpha_t \sim 1/200$. The FSL train is thus composed of individually dispersed fields lying, in general, in the temporal far field of $E_0(t)$. If we increase the mismatch δf_s further, the dispersed pulse width exceeds the train's period, and temporal Talbot effect is built again upon multiple pulse-to-pulse interference. These two regimes are illustrated in the simulation of Fig. 2.

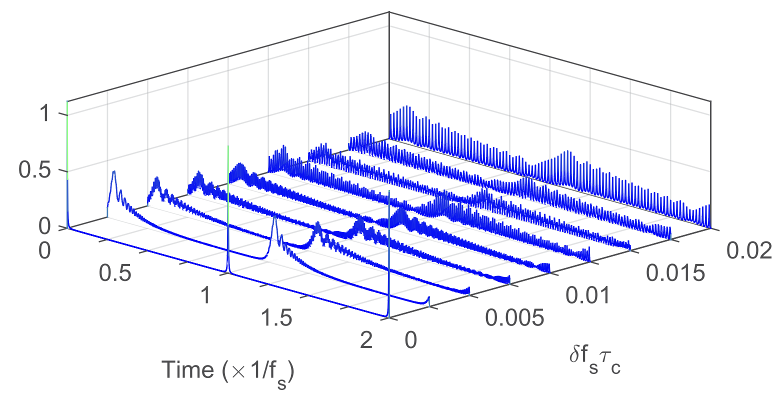

Fig. 2. Simulated intensity of an integer Talbot FSL field, Eq. (1), with an exponential spectrum, $g_n = \exp(-\kappa n)$ with $\kappa = 0.01$, for different values of $\delta f_s \tau_c$. At low values of the mismatch, $\delta f_s \tau_c = 0.0025$, the train comprises a series of dispersed pulses in the far field, but pulse-to-pulse interference is not yet noticeable. After this point, the intensity progressively reflects multiple pulse-to-pulse interference, leading to the $\delta f_s \tau_c = 1/q = 1/50$ fractional Talbot condition where the 50-fold increase in repetition rate is already perceptible.

3. FSL fields in the temporal Fraunhofer region

The objective of this section is to compute and analyze a uniform asymptotic expansion of the field in Eq. (6) in inverse powers of α_ν, and thus valid for all values of t. To ease the notation, the spectral Fresnel number will be denoted simply by α. We also introduce dimensionless variables as follows. The temporal extent of $E(t)$ in Eq. (6) can be estimated as $\Delta t = 2\pi\phi\Delta\nu$, as this quantity describes the difference in group delay between the most distant spectral components. We thus define the dimensionless frequency, $u = \nu/\Delta\nu$, time, $\tau = t/\Delta t$, spectrum, $G(u) = \Delta\nu\, g(u\Delta\nu)$, and envelope, $U(\tau) = E(\tau\Delta t)$. With these changes, the first expression in Eq. (6) rewrites:

$$U(\tau) = e^{j\pi\alpha\tau^2} \int_0^\infty du\, G(u) e^{-j\pi\alpha(u-\tau)^2} \tag{7}$$

This formula is the starting point of our analysis. Since for typical values $\alpha \equiv \alpha_\nu = 1/\alpha_t \sim 200$, it represents the temporal far field of the transform-limited pulse as the product of a chirp factor times the near field propagation of the spectrum $G(u)$. The asymptotic expansion of Eq. (7) provides a field description at large but finite values of α, and permits the interpretation of the fields as the combination of the standard Fraunhofer limit plus diffractive-like, higher-order effects associated to the near field propagation of the spectrum in the presence of a spectral edge.

The leading order of the expansion describes the field in the spectral near field limit $\alpha \to \infty$ in Eq. (7), equivalent to the temporal far field or Fraunhofer limit, and defines the so-called

Optics EXPRESS

frequency-to-time mapping where the wave's spectrum is mapped to the pulse's temporal envelope. This limit can be computed by recalling that the temporal Fresnel number satisfies the condition $\alpha_t \ll 1$, hence reducing the computation of the last part of Eq. (6) to a Fourier transform. Alternatively, it can be computed by use of the stationary phase approximation in Eq. (7) or in the first representation in Eq. (6). In either case, one gets an envelope composed of a linear chirp factor and a real amplitude given by the spectrum:

$$U_{go}(\tau) = \frac{e^{-j\pi/4}}{\sqrt{\alpha}} e^{j\pi\alpha\tau^2} G(\tau) \tag{8}$$

Using the terminology of diffractive optics, this approximation will be referred to as the geometrical optics (go) limit of the diffraction integral [34]. Notice that $U_{go}(\tau)$ is discontinuous at $\tau = 0$ due to the existence of a spectral edge and, in fact, it vanishes for $\tau<0$ because in this range the stationary phase point is outside the integration interval of Eq. (7). The frequency-to-time transformation is implicit in our dimensionless notation, since the field, in standard variables, is proportional to the time-mapped spectrum, $G(\tau) = \Delta\nu\, g(t/2\pi\phi)$. Note also that, although α is large, the phase prefactor in Eq. (7) describing the linear chirp decreases with dispersion, as the translation to dimensional variables reads $\exp(j\pi\alpha\tau^2) = \exp(jt^2/2\phi)$.

As shown in the Appendix, the asymptotic expansion of Eq. (7) to second order is given by:

$$\begin{aligned} U(\tau) &= U_{go}(\tau) + U_{edge}(\tau) + U_{slope}(\tau) + O(\alpha^{-3/2}) \\ &= U_{go}(\tau) + \frac{j}{2\pi\alpha}\frac{F(2\alpha\tau^2)}{\tau} G(0) + \frac{j}{2\pi\alpha}\left[F(2\alpha\tau^2) - 1\right] G'(0) + O(\alpha^{-3/2}) \end{aligned} \tag{9}$$

where function $F(x)$, defined for $x \geq 0$, is the modified Fresnel integral introduced by Kouyoumjian and Pathak in their uniform theory of diffraction [36]:

$$F(x) = j\pi\sqrt{x}e^{j\pi x/2} \int_{\sqrt{x}}^{\infty} dw\, e^{-j\pi w^2/2} \tag{10}$$

In this definition, the square roots are taken with positive sign, so that $\sqrt{y^2} = |y|$. The solution described by Eq. (9) depends on spectrum $G(u)$ through $U_{go}(\tau)$ and on two additional parameters, the spectrum amplitude and right slope at the edge, $G(0)$ and $G'(0) = dG/du|_{u=0+}$, respectively. When $G'(0) = 0$, the solution in Eq. (9) coincides, except for the global multiplicative chirp factor, with the near field originated by the diffraction of a straight edge [37]. These corrections to the geometrical optics field are originated locally, as they only depend on the existence and the slope of a spectral edge and not on the field's spectral width $\Delta\nu$. Borrowing again the nomenclature from diffraction theory, we will refer to the two additional terms in Eq. (9) as edge and slope diffraction terms [34], respectively, as introduced in the first part of the equation. The contributions to Eq. (9) are exemplified in Fig. 3.

The presence of $F(2\alpha\tau^2)$ in Eq. (9) leads to the identification of two temporal regimes in the solution. As explained in the Appendix, $F(x) \sim 1$ only for $x<1$. Therefore, in the region $2\alpha\tau^2<1$ or, in dimensional variables, in the temporal region $t^2<\pi\phi = \tau_c\delta f_s/(2f_s^2)$ describing the *pulse onset*, both edge and slope diffraction are significant, as shown in Fig. 3. In this region, function $F(2\alpha\tau^2)$ is linear in $|\tau|$ and of order $\sqrt{\alpha}$. Near the pulse onset, and in contrast to the slope diffraction field, the edge diffraction field represents a correction of the same order as the geometrical optics field, and discontinuous at $\tau = 0$:

$$U_{edge}(\tau) = \frac{jG(0)}{2\pi\alpha}\frac{F(2\alpha\tau^2)}{\tau} \sim -\frac{e^{-j\pi/4}}{2\sqrt{\alpha}} G(0)\,\mathrm{sign}(\tau) \qquad \text{for } \tau \to 0 \tag{11}$$

As shown in Fig. 3, this discontinuity compensates for that in $U_{go}(0)$ and results in a continuous total field. In the opposite regime $t^2>\pi\phi$, away from the pulse onset, $F(2\alpha\tau^2) \sim 1 + j/(2\pi\alpha\tau^2)$,

Optics EXPRESS

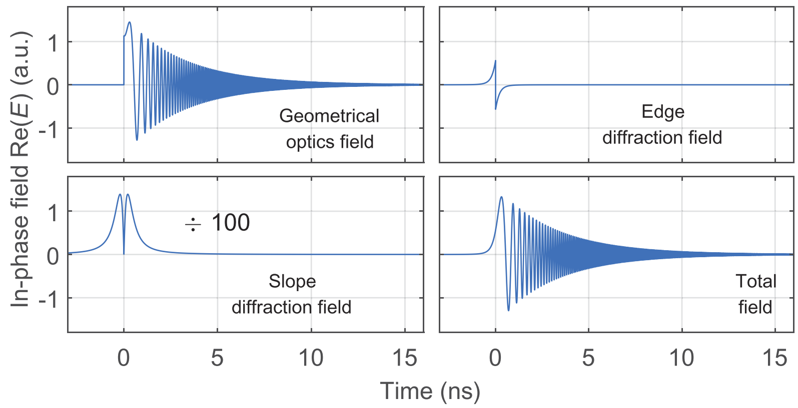

Fig. 3. Simulation of the contributions in Eq. (9) to the in-phase component Re $E(t)$ of the example field with exponential spectrum $g(f) = \exp(-f/\Delta\nu)$. The parameters are $f_s = 80.050$ MHz, $\Delta\nu = 8$ GHz, and $\tau_c = 50$ ns, so that $\delta f_s \tau_c = 0.0025$, $\phi = 62170\,\mathrm{ps}^2/\mathrm{rad}$, $\sqrt{\pi\phi}$ =0.44 ns, and $\alpha = 25$. The slope diffraction field has been magnified by a factor of 100.

and so the slope diffraction term becomes subleading and the edge diffraction tends to a slowly-decaying quadrature field, $U_{edge}(\tau) \sim jG(0)/(2\pi\alpha\tau)$. The total field is:

$$U(\tau{>}1/\sqrt{2\alpha}) \sim U_{go}(\tau) + j\frac{G(0)}{2\pi\alpha\tau} \qquad U(\tau{<}-1/\sqrt{2\alpha}) \sim j\frac{G(0)}{2\pi\alpha\tau} \tag{12}$$

For typical values of the FSL field period, ~10 ns, this second region is reached after a fraction of ns around $\tau = 0$, see Fig. 3.

The intensity of the total field is also plotted in Fig. 4(a), where the ripples are due to the interference between the *go* and the asymptotic edge field in the first formula of Eq. (12). In the absence of slope diffraction, the value of the relative intensity at $\tau = 0$ between the total field and its geometrical optics approximation is $|U(0+)|^2/|U_{go}(0+)|^2 = 1/4$, as in the diffractive optics solution of the straight edge [37]. Note also that this weak, slowly-decaying edge field always originates a certain level of pulse-to-pulse interference when the pulse is inside a pulse train, even if the overall dispersed pulse width does not exceed the train's period.

In Figs. 4(b)–4(c) we also plot the instantaneous frequency of this example field, whose different regimes can be explained as follows. Referring to Eqs. (8) and (12), if the FSL spectrum $G(\tau)$ is bandlimited or its time-mapped spectral decay rate is faster than that of the edge field, the total field for $\tau{>}1/\sqrt{2\alpha}$ becomes eventually dominated by the slowly decaying edge field, distorting the otherwise perfect linear chirp of the *go* term. The resulting phase patterns of the total field $U(\tau)$ are schematically described in Fig. 5. For small values of τ, the magnitude of $U_{go}(\tau)$ is greater than that of the edge field, which only induces a small shift of the center of $U_{go}(\tau)$, as shown in Fig. 5(a) with an orange point. Phasor $U(\tau)$ thus evolves following the blue circle, which represents the chirped phase of $U_{go}(\tau)$. The small component of the edge field induces a progressive oscillation in the chirped phase due to the pass of $U(\tau)$ near zero. In Fig. 5(b) the magnitude of the edge field is still lower than $U_{go}(\tau)$, but this last one has decreased to a comparable level. The previous phase oscillations transform into positive sharp jumps of variation π radians, but the phase still grows at every cycle of the geometrical optics phase. In Fig. 5(c), the $\pi/2$ phase of the edge field becomes dominant, and the phase evolves in the same cycle now with negative π phase jumps. Finally, when the magnitude of the geometrical optics field is much smaller than that of the edge field, we recover a series of oscillations over the $\pi/2$ phase. We refer to this effect as the *capture* of the geometrical optics phase by the phase in quadrature of the edge field, due to the close analogy with the capture effect in the demodulation

Optics EXPRESS

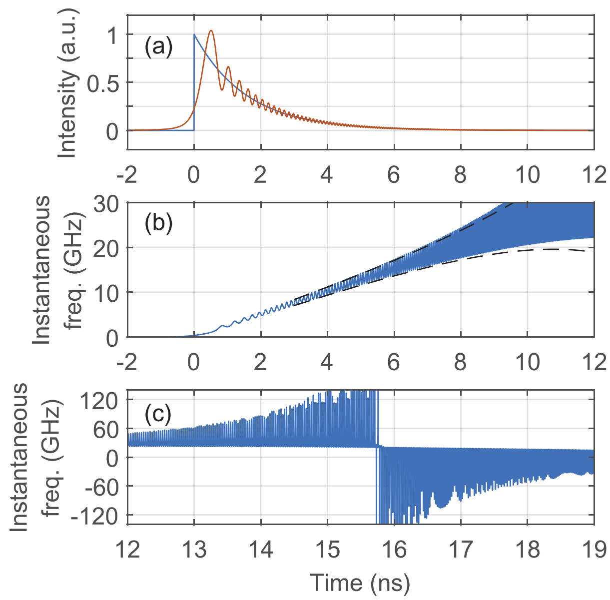

Fig. 4. Simulation of the (a) intensity and (b), (c) envelope's instantaneous frequency of the field with exponential spectrum. In (a): blue, intensity of the geometrical optics field $I_{go}(t) = |E_{go}(t)|^2$ and orange, intensity of the total field $I(t) = |E(t)|^2$. These intensities are normalized to the peak value of $I_{go}(t)$. In (b), the dashed black curves are the envelopes of the correction term to the chirp in Eq. (13).

of two interfering frequency-modulated radio stations of different power levels [38]. The capture point is defined by the transition between (b) and (c), where the phasors' magnitudes are similar.

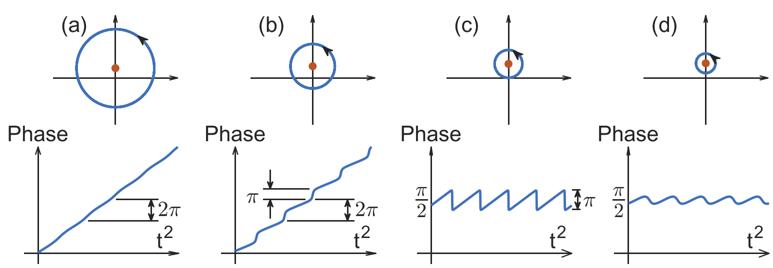

Fig. 5. Schematics of the temporal dependence of the phase when a phasor quadratic in time is superimposed to a constant phasor with different relative magnitudes. See the explanation in the text.

The capture effect also manifests itself in four different regimes of the instantaneous frequency. In the first regime of Fig. 5(a), the derivative of the phase is no longer linear, but shows progressive oscillations. As is shown in the Appendix, the instantaneous frequency in this regime is given by:

$$\omega_i(t) \simeq \frac{t}{\phi} - \frac{1}{\sqrt{2\pi\phi}} \frac{g(0)}{g(t/2\pi\phi)} \sin\left(\frac{t^2}{2\phi} - \frac{\pi}{4}\right) \tag{13}$$

Therefore, the instantaneous frequency presents a chirped frequency modulation whose amplitude is governed by the inverse of the time-mapped spectrum, $g(t/2\pi\phi)$, which is a decreasing function of time. As a consequence, the chirp does not evolve linearly, but in a series of progressive

Optics EXPRESS

oscillations whose amplitude increases along the pulse. The second regime of Fig. 5(b) results in the transformation of these oscillations in positive bumps, but the overall linear growth of the instantaneous frequency persists. These bumps arise from the π phase jumps which become progressively sharper, and so the values of the instantaneous frequency become larger. After the capture point, in Fig. 5(c), the bumps become negative and $\omega_i(t)$ drops progressively to zero. In the final regime of Fig. 5(d), the instantaneous frequency shows small oscillations near zero.

These regimes are illustrated in Figs. 4(b)–4(c) using our example field. In (b) we show the instantaneous frequency at the pulse's leading edge where the oscillations of the linear chirp are apparent. Superimposed are the envelopes of the second term in Eq. (13) which account for most of the effect, as expected. At a magnified scale, Fig. 4(c) shows the frequency at the far trailing edge, where the change of the bumps' sign is separated by the capture point at 15.8 ns.

The existence of this additional chirped frequency modulation with increasing amplitude and the subsequent capture of the phase by the edge field points to an intrinsic problem of the linear chirp generated by pulse dispersion in the far field when the source spectrum presents an edge. According to Eq. (13), the chirp linearity can be improved by equalizing the pulse spectrum so that, ideally, $g(f) \approx g(0)$. Even in this case, however, residual oscillations of amplitude $\Delta\omega_i = 1/\sqrt{2\pi\phi}$ remain. With respect to the capture effect, one can reduce the large bumps around the capture point by spectral filtering, so that $g(f)$ decreases sharply at $f \simeq \Delta\nu$ and thus reduces the capture region. Alternatively, one can reduce the diffractive contributions to the field, and therefore mitigate these effects, by use of an optical filter that smooths the spectral edge, at the expense, of course, of output optical power.

Finally, we provide the asymptotic expansion of the total FSL train, $U_{FSL}(\tau) = \sum_m U(\tau - m\tau_0)$, with $\tau_0 = T/\Delta t$ the dimensionless period. We first divide the edge field in its asymptotic limit of Eq. (12) plus a contribution localized at the pulse onset $2\alpha\tau^2 < 1$. Note that both are singular at $\tau = 0$, but the divergences cancel each other:

$$U_{edge}(\tau) = U_{edge}^{(asymp)}(\tau) + U_{edge}^{(local)}(\tau) = \frac{j}{2\pi\alpha}\frac{G(0)}{\tau} + \frac{j}{2\pi\alpha}\frac{G(0)}{\tau}\left[F(2\alpha\tau^2) - 1\right] \tag{14}$$

Defining $U_{local}(\tau) = U_{edge}^{(local)}(\tau) + U_{slope}(\tau)$, which describes the local contributions at the pulse onset, the FSL train can be written as:

$$U_{FSL}(\tau) = \sum_{m=-\infty}^{\infty}\left[U_{go}(\tau - m\tau_0) + U_{local}(\tau - m\tau_0)\right] + \frac{jG(0)}{2\alpha\tau_0}\cot\left(\pi\frac{\tau}{\tau_0}\right) + O(\alpha^{-3/2}) \tag{15}$$

where we have used the Mittag-Leffler expansion $\pi\cot(\pi z) = \sum_{k=-\infty}^{\infty}(z+k)^{-1}$ [39] to sum the infinite series of asymptotic edge fields.

4. Experimental results and model fitting

We performed specific measurement to provide experimental confirmation of the theory described by Eqs. (4), (9) and (15). The experimental setup is similar to that of [16], which was based on a cw seed laser at 1550 nm and an AOFS operating at ~80 MHz. The loop's round-trip time was $\tau_c = 73.202$ ns, inferred from a fit of the acousto-optic shifting frequencies f_{s0} leading to different fractional Talbot conditions. The TBPF bandwidth (Exfo, XTM-50) was $\Delta\nu \simeq 20$ GHz, and the resulting power decay was 0.026 dB/line in the band dc-16 GHz. As is schematically shown in Fig. 1, single-detector, self-heterodyne measurements were carried out by mixing the FSL output with a portion of the seed laser, followed by wideband (40 GHz) detection and recorded by a 20 GHz DSO (sampling rate 40 GS/s, depth of 8 bits). The heterodyne signal is given by

$$v(t) = E_{LO}^2 + 2E_{LO}\mathrm{Re}\left[e^{-j\varphi}E_{FSL}(t)\right] + |E_{FSL}(t)|^2 \tag{16}$$

with E_{LO} the local oscillator's (LO) amplitude and φ the LO phase. By maximizing E_{LO}, the self-heterodyne trace provides a measurement of the field at the LO angle, $\mathrm{Re}[e^{-j\varphi}E_{FSL}(t)]$. The

Optics EXPRESS

relative value of the amplitude ratio $E_{LO}/(\max|E_{FSL}|)$ is ~10, inferred from our first experimental result shown in Fig. 6 described below. The traces were recorded in a time interval of 20 ms using the entire DSO's memory, for a total of ~1600 periods of the optical train.

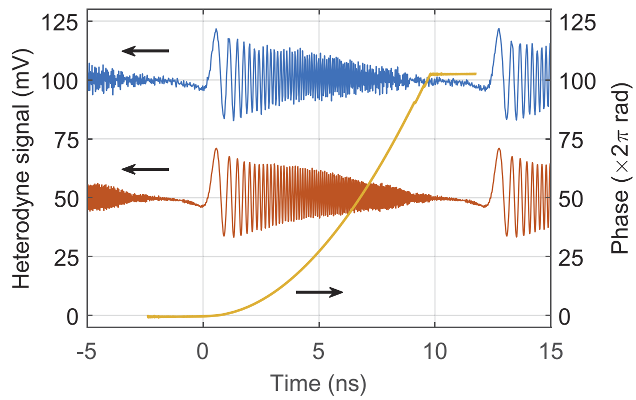

Fig. 6. Blue: raw heterodyne signal of the chirped FSL field obtained by detuning the shifting frequency of the $p = 6$ integer Talbot condition. Orange: chirped train after denoising, shifted −50 mV to ease the comparison. Yellow: unwrapped phase of a single period in the denoised train.

4.1. Chirped integer Talbot field

In a first experiment, we set the FSL at a shifting frequency $f_s = 82.018$ MHz, above the shifting frequency $f_{s0} = 81.975$ MHz of the integer Talbot condition with $f_s\tau_c = 6$, so that $\delta f_s\tau_c = 0.003$. A portion of the raw trace is shown in blue in Fig. 6, where the dispersion-induced chirp is apparent. We first computed the discrete Fourier transform of this raw signal, obtaining the FFT spectrum shown in Fig. 7(a) with a blue trace. This trace represents the optical spectrum g_n^2 of the comb lines above the injection-seed wavelength, except for the line at dc, which is larger due to the constant term in Eq. (16), and also near dc, due to the $|E_{FSL}(t)|^2$ term. The spectral lines are clearly resolvable as a result of the large number of recorded periods. The spectrum is, however, aliased at 20 GHz due to the DSO bandwidth, which roughly coincides with the TBPF spectral width. At this point, we optimized the nominal value of f_s to the Hz level by maximizing the total power contained in the harmonics using spline interpolation of the FFT trace. This was necessary in order to provide an exact time reference along the whole pulse train.

The spectral lines can be isolated in the aliased spectrum using the fact that they are multiple of the shifting frequency f_s, as shown in the zoom view near the Nyquist frequency of Fig. 7(b). This way, the effective detection bandwidth was extended up to 25 GHz resulting in a total of 304 lines. Afterwards, noise was removed by a 4-MHz bandpass filter around each spectral line implemented with a Kaiser-Bessel window with $\beta = 6$, also shown in Fig. 7(b). This denoising step, equivalent to a running temporal average over ~40 FSL periods, reduces not only the wideband detection noise but also the quantization noise originally present in the DSO trace. After inverse Fourier transform, a portion of the denoised time-domain waveform is shown in Fig. 6 with an orange trace, shifted −50 mV to ease the comparison. In these traces the sampling rate was extended to 80 GS/s. Then, the complex field was retrieved using the same procedure as in [16], first subtracting the dc value and then performing the Hilbert transform by removing the negative frequencies in the FFT spectrum. This allowed the numerical determination of the phase, shown in units of cycles with yellow trace for the sample pulse of Fig. 6, and also of the instantaneous frequency, for which the maximum detectable frequency is 40 GHz after the bandwidth extension procedure described above.

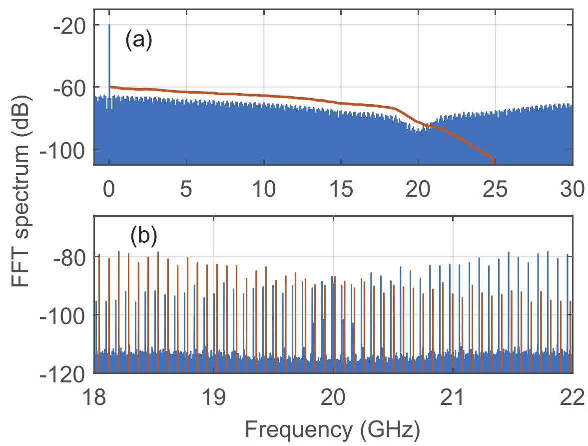

Fig. 7. (a) FFT spectrum of the raw heterodyne signal (blue trace), and smoothed spectrum used in the simulations (orange trace). (b) Zoom of the FFT spectrum around the Nyquist frequency (blue trace), and filtered spectral lines (in orange).

The experimental instantaneous frequency is presented in Fig. 8 with blue traces. In Fig. 8(a) it is observable a linear chirp rate of 2.2 GHz/ns associated to a dispersion $\phi = 73082\,\mathrm{ps}^2/\mathrm{rad}$, which deviates 1.8% from the value $\phi = \tau_c \delta f_s/(2\pi f_s^2) = 74424\,\mathrm{ps}^2/\mathrm{rad}$ estimated using the cavity's round-trip time τ_c. The predicted progressive oscillations are clearly observable in the zoom view of the leading edge of Fig. 8(b). The amplitudes of these initial oscillations around the linear tendency are ±220 MHz, in good agreement with our estimate $\Delta\omega_i/(2\pi) = 235\,\mathrm{MHz}$. In Fig. 8(a), these oscillations become positive and negative bumps with large amplitudes due to the change in slope of the time-mapped spectrum after 18.4 GHz (see Fig. 7(a)), reaching the capture point at 9.8 ns. After this point, the instantaneous frequency suddenly drops.

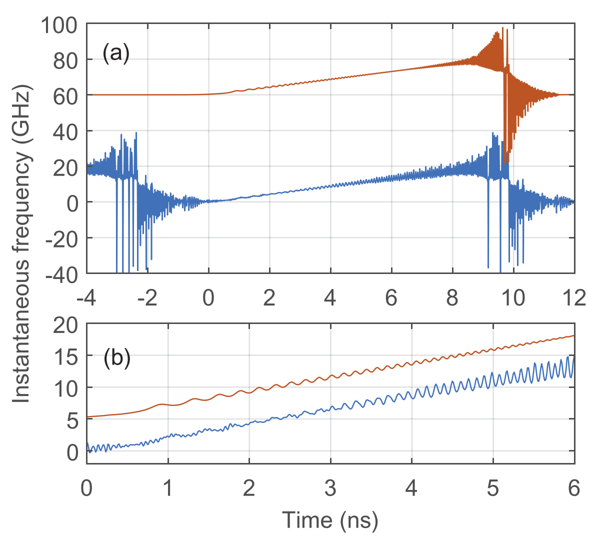

Fig. 8. (a) Instantaneous frequency of the chirped pulse after denoising (blue trace) and of the reconstructed field (orange trace, shifted +60 GHz). (b) Zoom of the instantaneous frequency in the leading edge. The reconstructed instantaneous frequency is shifted +5 GHz.

Optics EXPRESS

The capture effect can also be observed in the heterodyne signal of Fig. 9, zoomed from Fig. 6. In terms of the phase, the capture point is determined by the instant when the phase ceases to grow quadratically, and is associated with a decrease in the high-frequency oscillations of the heterodyne signal, as is apparent in both the raw and denoised traces of that figure.

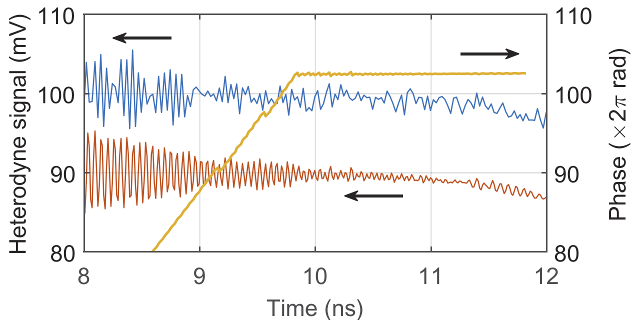

Fig. 9. Zoom of Fig. 6 near the capture point: raw heterodyne signal of the chirped FSL field (blue trace) and denoised signal (orange, shifted −10 mV). In yellow, phase of the denoised chirped FSL field.

4.2. Model fitting

The chirped Talbot field was then globally compared with the models described in Eqs. (9) and (15) using a reconstructed optical spectrum and the fit of the defining parameters. As for the spectrum, we estimated the spectral function $g(f)$ from the comb amplitudes g_n in Fig. 7, first smoothing these samples by a low-pass filter and then forcing the edge at zero frequency by extrapolating the values of g_n from $n = 4$ to $n = 7$ towards $n = 0$. This was necessary since the heterodyne signal, Eq. (16), contains the FSL intensity, $|E_{FSL}(t)|^2$, which makes its contribution to the FFT spectrum near dc. The smoothed spectrum is shown in Fig. 7(a) in orange trace. This spectrum thus defines the function $g(f)$ and so the coefficients $G(0)$ and $G'(0)$ in Eqs. (9) and (15) up to a constant, referred to as the FSL amplitude in what follows.

The complex form of the denoised field was then fitted to the model of Eq. (15) by optimizing in independent steps the values of global dispersion ϕ, FSL amplitude, LO phase φ, and the initial pulse time for a sample period of the experimental FSL train. Dispersion was first determined by fitting the experimental phase, shown with yellow trace in Fig. 6, to a quadratic function in the central part of the pulse, where the influence of edge fields arising from the same pulse or its neighbour pulse can be neglected.

Subsequently, we carried out an estimation of the initial time by minimizing the difference between the experimental and the theoretical instantaneous frequency extracted from Eq. (15), since it does not depend neither on the FSL amplitude nor on the LO phase. Finally, FSL amplitude and LO phase were fitted to a period of the full theoretical FSL train, Eq. (15), from the reconstructed optical spectrum and the previous estimates of initial time and dispersion, searching for the minimum rms error between experimental and theoretical heterodyne signals. This search was restricted to the leading edge of the waveform, between −2 ns and 1 ns, since the depth of the field's first valley and the height of its first hill are particularly sensitive to these parameters.

The reconstructed optical waveform is shown in Fig. 10(a) with an orange trace, superimposed to the denoised and dc-free experimental signal in blue. Here we have taken into account the pulse-to-pulse interference with the following pulse, as is reflected in the decreasing trailing edge after 12 ns. Despite the approximations involved and the complexity of the waveform, the global agreement is remarkable. As shown in Fig. 10(b), the peak-to-peak difference between

Optics EXPRESS

experimental and reconstructed phases is less than half a cycle for a total of 103 oscillations of the waveform's phase in one period.

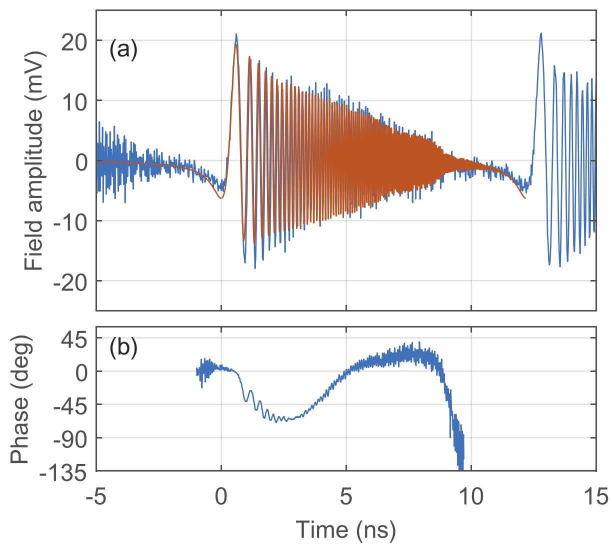

Fig. 10. (a) Heterodyne signal after denoising (blue trace) and reconstructed field (orange trace). (b) Phase difference between the heterodyne and the reconstructed signals.

Also illustrative is the reconstruction of the instantaneous frequency, shown in Fig. 8 with orange traces, where the predicted overall slope, the initial chirp oscillations, magnified in Fig. 8(b), and the capture point at 9.8 ns are well described by the theory. In contrast to the example field of Fig. 4, however, the capture is not realized by the edge field originated at $t = 0$, but by the closer edge field of the following chirped pulse whose onset is at $T = 1/f_s = 12.2$ ns. This observation is analyzed with more detail in the Appendix.

The summation in Eq. (15) of pulse-to-pulse interference terms also implies that the quadrature field responsible for the capture effect vanishes somewhere around the center of the pulse's period since the edge fields of neighbour pulses have opposite sign at both sides of their respective edges, see Fig. 3. This is the reason why, in the simulations in Fig. 8, the amplitude of the oscillations progressively decreases, reaches a minimum at ~7 ns, and subsequently grows towards the capture point. This behaviour, however, is not reflected in the experimental trace, where the instantaneous frequency shows oscillations and bumps with a continuously increasing amplitude. We have not a definite explanation of this discrepancy, which can be due to the acquisition procedure, based on the single-detector heterodyne signal which only represents an approximation to the in-phase field, or to the analysis method that includes a spectral filtering equivalent to a time average. In any case, the presented model correctly predicts the main properties observed in the field phase, namely, the oscillations and bumps of the linear chirp and the existence of capture effect in the pulse's trailing edge.

4.3. Phases of the chirped fractional Talbot field

In a second experiment, we targeted the determination of the Talbot phases at fractional Talbot conditions using chirped pulses. We introduced a small mismatch in the acousto-optics shifting frequency corresponding to fractional Talbot indices of the form $(q-1)/q$ with $q = 3, 6$ and 12 over the $p = 5$ integer Talbot condition, so that the heterodyne signals were composed of a series of q chirped pulses per period. In Fig. 11 we present, as an example, the raw heterodyne trace of a chirped 2/3 Talbot field, distributed in three pulses of duration $T/3$ in a period of $T = 12.9$

Optics EXPRESS

ns. The phase terms associated to these Talbot 2/3 conditions are, respectively, 1, $\exp(j2\pi/3)$, and $\exp(j2\pi/3)$ and therefore the train is arranged in a pattern composed of two equal pulses followed by a different pulse, easily distinguishable in the figure by their leading edges. The use of chirped pulses instead of the transform-limited pulses of the perfectly matched fractional Talbot condition not only facilitates this visual identification of the pattern, but also helps its correlation detection, as explained below.

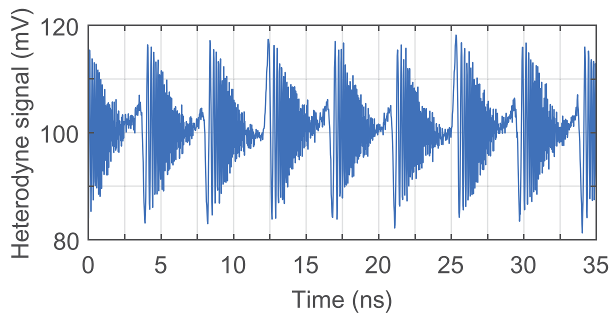

Fig. 11. Raw heterodyne signal of the chirped Talbot 2/3 field (f_s = 77.435 MHz).

The Talbot phase terms $\Phi_n = \exp(j\pi s n^2/q)$ $(n = 0, \ldots q-1)$ carried by the n-th pulse within the basic period, at or near the $(q-1)/q$ fractional Talbot condition are given by [26,33]:

$$\Phi_n = \exp[j\pi(q-1)n^2/q] = (-1)^n \exp(-j\pi n^2/q) \tag{17}$$

The experimental determination of these phases proceeds as follows. Once generated and recorded, the traces were denoised, dc filtered, Hilbert transformed, and finally Fourier transformed back to the time domain in the form of denoised complex envelopes. A digital correlator was used to compare each of the q pulses in a period with the $n = 0$ reference pulse, $E_{ref}(t)$, according to:

$$C(u) = \int_0^{T/q} dt\, E^*_{ref}(t) E_{FSL}(t+u) \tag{18}$$

This way, the complex cross-correlation $C(u)$ shows a series of peaks at intervals T/q whose complex values include a phase term with the sought-for difference between the pulse and reference phase terms, $C(u = nT/q) \sim \exp\left(j\pi s n^2/q\right)$ with $n = 0, 1, \ldots, q-1 \mod q$. In practice, and since these chirped pulses always show a certain level of pulse-to-pulse interference, the reference pulse $E_{ref}(t)$ was chosen as the central part of the $n = 0$ chirped pulse in the pulse train, with a width of $T/(3q)$ for each of the quoted values of q.

The experimental results are shown in the constellations of Fig. 12, together with the theoretical Gauss phases, Eq. (17). Each constellation includes ten different samples per phase level randomly picked among the 1600 periods of the recorded pulse train. Since these complex samples are normalized to unit amplitude, Talbot conditions with higher q index, which distribute the same optical power in pulses of duration T/q, show a lower signal-to-noise ratio and therefore a higher spread in the constellation. The agreement of the experimental and theoretical values is, however, excellent. The rms Error Vector Magnitudes of the constellations, computed for a total of 1000 samples per phase level, are EVM_{rms} = 3.4%, 5.5%, and 9.1% for Talbot 2/3, 5/6, and 11/12, respectively. This result confirms the passive generation of pulse trains following the Gauss sequences by temporal Talbot effect.

Optics EXPRESS

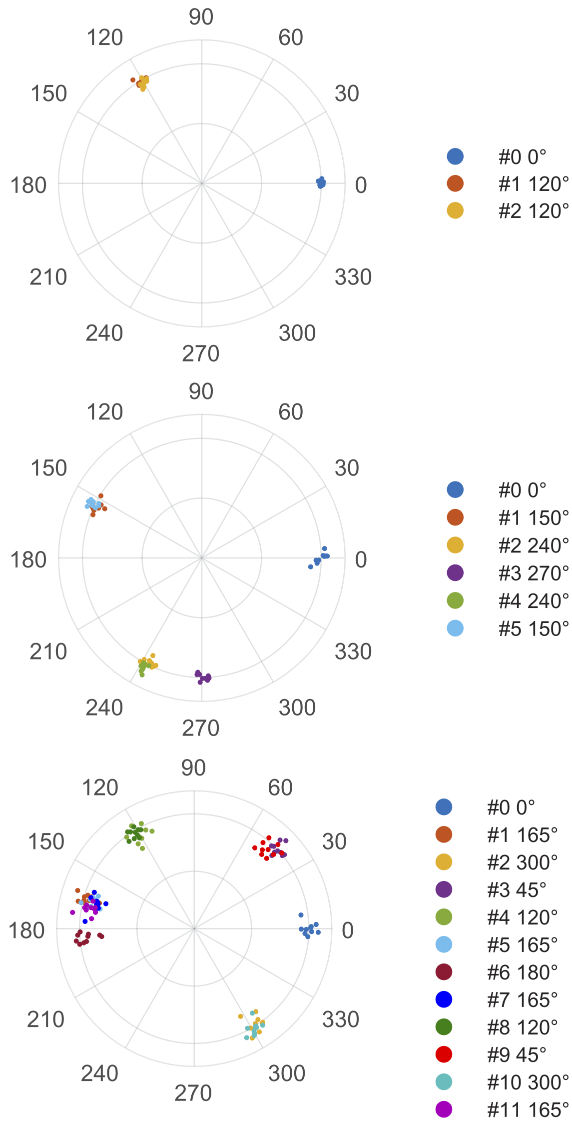

Fig. 12. Experimental $(q-1)/q$ Talbot phases (left plot) and corresponding Gauss phases $\Phi_n = \exp[j\pi(q-1)n^2/q]$ with $n = 0, \ldots, q-1$ (right legend). From top to bottom, Talbot 2/3 (f_s = 77.435 MHz), Talbot 5/6 (f_s = 79.706 MHz), and Talbot 11/12 (f_s = 80.841 MHz).

5. Conclusions

We have presented a theoretical and experimental investigation of the chirped optical fields generated in acousto-optic FSL by a detuning of the AOFS frequency from the integer and fractional Talbot conditions. Our results demonstrate the equivalence of the Talbot phases generated at fractional conditions with the Gauss sequences, and identify novel properties of the generated chirps. An asymptotic model of the field in the temporal Fraunhofer domain has been constructed, which describes several deviations from the standard frequency-to-time mapping description of the far field. The model accounts for the existence of ripples in the pulse intensity,

Optics EXPRESS

unavoidable pulse-to-pulse interference in the pulse train, small oscillations in the expected linear pulse chirp, and the capture of the phase at its trailing edge by the adjacent pulse. These features are due to the existence of corrections to the geometrical optics field originated by the FSL's spectral edge, in analogy to the diffraction of a straight edge. The experimental results have been enabled by a proper processing of the heterodyne signal, which includes denoising, bandwidth extension, and Hilbert transform.

From the practical point of view, these outcomes identify general properties of acousto-optic FSL or lasers. First, the existence of a spectral edge leads to pulses with a slow decay $\sim 1/t$, either transform-limited or chirped, and therefore to a certain level of pulse-to-pulse interference. This interference may affect both the amplitude and the phase of the individual pulses in the train and, in particular, may originate large pulse-to-pulse amplitude fluctuations at or near fractional Talbot conditions with high q factors of increase in repetition rate, where pulse overlap is expected to be larger. The same observation applies to systems at integer Talbot conditions fed by different seed wavelengths for its use as signal processors or signal generators [11]. Here, what is exploited is the loop's ability to provide a wavelength-to-time mapping from the input wavelengths to the delays where the corresponding Talbot pulses are outputted. The temporal profile of these transform-limited pulses represents the system's impulse response and, therefore, their slow asymptotic decay, although does not affect the resolution, may originate crosstalk or averaging effects in the output. In either case, these effects can be mitigated or even totally suppressed by a proper optical filter that smooths the spectral edge, thus avoiding the edge fields responsible of the slow pulse asymptotic decay at the expense of resolution and output power.

Second, our results also point out a generic limitation of the linear chirps generated by FSL in the Fraunhofer region, as they show oscillations and phase capture due to the interference of the geometrical optics and edge fields. As discussed in Section 3, these effects can be mitigated by using equalized FSL spectra, as in [13], and again can be totally avoided by optical filtering the spectral edge. Finally, we point out that the FSL systems based on the spectrum of the frequency comb are not affected by these shortcomings, since in these cases the spectral phase, responsible of the temporal form of the output pulses, is either calibrated, as in high-resolution spectroscopy systems [8,10], or simply plays no role, as in pulse-compression laser range finders based on digital correlation techniques [16].

6. Appendix. Asymptotic expansions

The computation of Eq. (9) relies on standard results of uniform asymptotic theory [40,41], but expressed in a form, using the modified Fresnel integral $F(x)$, Eq. (10) [36], that simplifies the description of the different temporal scales involved in the problem. The expansion in Eq. (9) can be derived directly, for instance, from the specialization of the results in [34]. Instead, we present here a compact derivation allowed by the simplicity of the quadratic phase in the integral of Eq. (7). We begin with a description of the relationship between the Fresnel integral and $F(x)$. The Fresnel integral used here is the complex conjugated of the standard expression [37]:

$$Z(v) = \int_0^v dw\, e^{-j\pi w^2/2} \tag{19}$$

With this definition, the locus of $Z(v)$ in the complex plane, or Cornu spiral, evolves from the second quadrant for $v \to -\infty$ to the fourth quadrant for $v \to +\infty$. As is well known, $Z(-v) = -Z(v)$, and the evolution of the Fresnel integral near the limit points of the Cornu spiral is described by an asymptotic expansion of the form:

$$Z(v) = \text{sign}(v)\frac{e^{-j\pi/4}}{\sqrt{2}} + \frac{j}{\pi v}e^{-j\pi v^2/2}\left(1 + \frac{j}{\pi v^2} + O(v^{-4})\right) \tag{20}$$

for $v \longrightarrow \pm\infty$. In fact, all the terms in parentheses depend on variable v^2. This observation justifies the definition of the modified Fresnel integral as [36]:

$$Z(v) = \mathrm{sign}(v)\frac{e^{-j\pi/4}}{\sqrt{2}} + \frac{j}{\pi v} e^{-j\pi v^2/2} F(v^2) \tag{21}$$

from which the integral expression of Eq. (10) follows directly. This formula represents $Z(v)$ for positive and negative arguments, $v{>}0$ and $v{<}0$, showing that the functional form in these two regimes only differs in the sign of the corresponding limit point. Therefore, $F(v^2)$ represents a parametrization of the Fresnel integral such that, when v^2 is large and thus $F(v^2) \approx 1$, the Cornu spiral is already approaching the limit point as the $1/v$ asymptote. In the limit $v^2 \longrightarrow 0$, function $F(v^2)$ behaves as $\sim |v|$, and represents the central region of the Cornu spiral. As is also well known [37], the transition between these two regimes occurs at $|v| \sim 1$. We recall that Eq. (11) gives the correct value $Z(0) = 0$ in both limits $v \longrightarrow 0\pm$ of the the representation in Eq. (21), since the discontinuity in $F(v^2)/v$ cancels that of $\mathrm{sign}(v)$.

In the asymptotic expansion of Eq. (7) we will make use of the following integrals:

$$\mathcal{I}_{n,\epsilon}(\tau) = \int_0^\infty du\, u^n\, e^{-\epsilon u^2}\, e^{-j\pi\alpha(u^2-2u\tau)} \tag{22}$$

with $n = 0, 1$ and $\epsilon \longrightarrow 0+$. In particular, $\mathcal{I}_{0,\epsilon}(\tau)$ reduces to a Fresnel integral for $\epsilon = 0$:

$$\mathcal{I}_{0,0}(\tau) = \frac{e^{j\pi\alpha\tau^2}}{\sqrt{2\alpha}}\left[\frac{e^{-i\pi/4}}{\sqrt{2}} + Z(\tau\sqrt{2\alpha})\right] = \frac{e^{j\pi\alpha\tau^2-i\pi/4}}{2\sqrt{\alpha}}\left[1 + \mathrm{sign}(\tau)\right] + \frac{j}{2\pi\alpha}\frac{F(2\alpha\tau^2)}{\tau} \tag{23}$$

and for $\mathcal{I}_{1,\epsilon}(\tau)$ we find, after integration by parts:

$$\mathcal{I}_{1,\epsilon}(\tau) = \frac{j\pi\alpha}{\epsilon + j\pi\alpha}\tau\mathcal{I}_{0,\epsilon}(\tau) + \frac{1}{2(\epsilon + j\pi\alpha)} \tag{24}$$

and so $\mathcal{I}_{1,\epsilon\rightarrow 0+}(\tau) = \tau\mathcal{I}_{0,0}(\tau) - j/(2\pi\alpha)$. We first derive the asymptotic expansion of field, Eq. (9). In a separate subsection we present the computation of the instantaneous frequency.

A.1. Optical field

The expansion of the integral in Eq. (7) at large α depends on its stationary phase point $u = \tau$ for $\tau \geq 0$ and the endpoint $u = 0$, critical points that colaesce for $\tau \longrightarrow 0$. A uniform asymptotic expansion, valid for $\tau \geq 0$, can be derived as follows [41]. We first write $G(u) = G(\tau) + [G(u) - G(\tau)]$ and divide the integral as $U(\tau) = U_1(\tau) + U_2(\tau)$. The first field is $U_1(\tau) = G(\tau)\,\mathcal{I}_{0,0}(\tau)$, and

$$U_2(\tau) = e^{j\pi\alpha\tau^2}\int_0^\infty du\,\left[G(u) - G(\tau)\right] e^{-j\pi\alpha(u-\tau)^2} \tag{25}$$

which is expected to be of higher order in the expansion since its stationary phase approximation vanishes. Integrating by parts, we get:

$$U_2(\tau) = \frac{j}{2\pi\alpha}\frac{G(0) - G(\tau)}{\tau} - \frac{j}{2\pi\alpha}\int_0^\infty du\,\frac{d}{du}\left(\frac{G(u) - G(\tau)}{u - \tau}\right) e^{-j\pi\alpha(u^2-2u\tau)} \tag{26}$$

The second term contributing to $U_2(\tau)$ is of higher order in the expansion since its stationary phase value is $G''(\tau)e^{-j\pi/4}/(j2\pi\alpha^{3/2})$. Neglecting this contribution and using Eq. (23) we get:

$$U(\tau) = U_1(\tau) + U_2(\tau) \sim U_{go}(\tau) + \frac{j}{2\pi\alpha\tau}\left[G(0) + G(\tau)\left(F(2\alpha\tau^2) - 1\right)\right] \tag{27}$$

We now recall that $F(2\alpha\tau^2) - 1$ is not null only in the vicinity of $\tau = 0$, specifically for $|\tau|{<}1/\sqrt{2\alpha} \ll 1$. Approximating $G(\tau) = G(0) + \tau\, G'(0) + \cdots$ in Eq. (27) we recover Eq. (9)

[34]. The following term in this expansion, $\tau^2 G''(0)/2$, gives a field of order τ/α, and since it is significant only for $|\tau|<1/\sqrt{2\alpha}$, represents again a subleading correction of $O(\alpha^{-3/2})$.

For $\tau<0$, the integral in Eq. (7) does not enclose the stationary point, and therefore its value is dominated by the behaviour of $G(u)$ near the endpoint $u = 0$ where the phase oscillates at a lower rate. To extract the asymptotic contributions of edge and slope, we decompose again $U(\tau)$ by writing $G(u) = H_\epsilon(u) + [G(u) - H_\epsilon(u)]$ with $H_\epsilon(u) = [G(0) + uG'(0)]\exp(-\epsilon u^2)$ for $u \geq 0$ and zero otherwise, and consider the limit $\epsilon \to 0+$. We find $U_1(\tau) = G(0)\mathcal{I}_{0,0}(\tau) + G'(0)\mathcal{I}_{1,\epsilon\to 0+}(\tau)$ which, using Eqs. (23) and (24), yields Eq. (9) for $\tau<0$. After integration by parts, field $U_2(\tau)$ is shown to be $O(\alpha^{-3})$, and thus subleading, in the limit $\epsilon \to 0+$.

A.2. Instantaneous frequency

The instantaneous frequency of the chirped pulse train $E_{FSL}(t)$ or $U_{FSL}(\tau)$ can be computed as the imaginary part, $\mathrm{Im}(\cdot)$, of its logarithmic derivative:

$$\omega_i(t) = \mathrm{Im}\left(\frac{1}{E_{FSL}(t)}\frac{dE_{FSL}}{dt}\right) = \frac{1}{\Delta t}\mathrm{Im}\left(\frac{1}{U_{FSL}(\tau)}\frac{dU_{FSL}}{d\tau}\right) \tag{28}$$

The region of interest in Eq. (28) is one period of the FSL train, $0<t<T$ or $0<\tau<\tau_0$. $U_{FSL}(\tau)$ is given by Eq. (15), and for $U'_{FSL}(\tau) = \sum_m U'(\tau - m\tau_0)$ we have:

$$U'(\tau) = 2\pi j\alpha \int_0^\infty uG(u)e^{-j\pi\alpha(u^2-2u\tau)}du \tag{29}$$

The asymptotic expansion of Eq. (29) is also given by Eq. (9) but referred to a new, edge-free, spectrum $\widetilde{G}(u) = uG(u)$, so that $\widetilde{G}(0) = 0$ and $\widetilde{G}'(0) = G(0)$. The contributions to $U'(\tau)$ from the integral in Eq. (29) are thus $\tau U_{go}(\tau) = \tau G(\tau)e^{j\pi\alpha\tau^2 - j\pi/4}/\sqrt{\alpha}$, which gives rise to the exact linear chirp, plus a localized field $G(0)\left(F(2\alpha\tau^2) - 1\right)$, but not of an edge-like field. Therefore, the numerator of Eq. (28) does not show pulse-to-pulse interference. Neglecting the local fields in both numerator and denominator, the instantaneous frequency can be compactly written as:

$$\omega_i(t) = 2\pi\Delta\nu\,\tau\,\mathrm{Re}\left[\left(1 + j\frac{e^{-j\pi\alpha\tau^2+j\pi/4}}{2\sqrt{\alpha}\tau_0}\frac{G(0)}{G(\tau)}\cot\left(\pi\frac{\tau}{\tau_0}\right)\right)^{-1}\right] \tag{30}$$

This equation allows for the discussion of the different properties of $\omega_i(\tau)$ for $2\alpha\tau^2>1$, as the local fields are not included. In the pulse's leading edge ($\tau \ll \tau_0$) we can approximate $\cot(\pi\tau/\tau_0) \sim \tau_0/(\pi\tau)$ and, after expanding the ratio in Eq. (30) to first order as $(1 + x)^{-1} \simeq 1 - x$, Eq. (13) follows. Second, the capture point τ_* is given by:

$$G(\tau_*) = \frac{G(0)}{2\sqrt{\alpha}\tau_0}\left|\cot\left(\pi\frac{\tau_*}{\tau_0}\right)\right| \tag{31}$$

The solution is located at a point τ_* where $G(\tau)$ is small compared to $G(0)$, and thus in the trailing edge of the pulse where $(\pi/\tau_0)\cot(\pi\tau/\tau_0) \sim 1/(\tau - \tau_0)$, so that the capture is carried out by the edge field of the following pulse. Third, if the spectrum is equalized, $G(\tau) \simeq G(0)$, the solution is located at the sharp end of the pulse where the geometrical optics field vanishes. In this case, the capture is almost instantaneous and the progressive increase of oscillation's amplitudes in the instantaneous frequency is not expected to be observed. Finally, the field responsible of the capture is $\cot(\pi\tau/\tau_0)$, which represents the sum of pulse-to-pulse interference terms due to edge fields. This capture field vanishes at $\tau = \tau_0/2$ or $t = T/2$, in the middle of the FSL period. At this point one expects a decrease in the linear chirp oscillations as shown in our simulation of Fig. 8.

Funding

Agencia Estatal de Investigación (TEC2017-89688-P); Association Nationale de la Recherche et de la Technologie (ANR-14-CE32-0022).

Disclosures

The authors declare no conflicts of interest.

References

1. H. Guillet de Chatellus, O. Jacquin, O. Hugon, W. Glastre, E. Lacot, and J. Marklof, "Generation of ultrahigh and tunable repetition rates in cw injection-seeded frequency-shifted feedback lasers," Opt. Express **21**(13), 15065–15074 (2013).
2. H. Guillet de Chatellus, E. Lacot, W. Glastre, O. Jacquin, and O. Hugon, "Theory of Talbot lasers," Phys. Rev. A **88**(3), 033828 (2013).
3. P. Coppin and T. G. Hodgkinson, "Novel optical frequency comb synthesis using optical feedback," Electron. Lett. **26**(1), 28–30 (1990).
4. K.-P. Ho and J. M. Kahn, "Optical frequency comb generator using phase modulation in amplified circulating loop," IEEE Photonics Technol. Lett. **5**(6), 721–725 (1993).
5. P. Shen, N. J. Gomes, P. A. Davies, P. G. Huggard, and B. N. Ellison, "Analysis and demonstration of a fast tunable fiber-ring-based optical frequency comb generator," J. Lightwave Technol. **25**(11), 3257–3264 (2007).
6. L. Wang and S. LaRochelle, "Talbot laser with tunable GHz repetition rate using an electro-optic frequency shifter," in *CLEO 2017 - Conference on Lasers and Electro-Optics, OSA Technical Digest* (Optical Society of America, 2017), paper JW2A.66.
7. H. Yang, M. Vallet, H. Zhang, C. Zhao, and M. Brunel, "Pulse doublets generated by a frequency-shifting loop containing an electro-optic amplitude modulator," Opt. Express **27**(13), 18766–18775 (2019).
8. V. Durán, C. Schnébelin, and H. Guillet de Chatellus, "Coherent multi-heterodyne spectroscopy using acousto-optic frequency combs," Opt. Express **26**(11), 13800–13809 (2018).
9. T. Chen, W. Kong, H. Liu, and R. Shu, "Frequency-stepped pulse train generation in an amplified frequency-shifted loop for oxygen A-band spectroscopy," Opt. Express **26**(26), 34753–34762 (2018).
10. V. Durán, L. Djevarhidjian, and H. Guillet de Chatellus, "Bidirectional frequency-shifting loop for dual-comb spectroscopy," Opt. Express **44**(15), 3789–3792 (2019).
11. H. Guillet de Chatellus, L. Romero-Cortés, and J. Azaña, "Optical real-time Fourier transformation with kilohertz resolution," Optica **3**(1), 1–8 (2016).
12. C. Schnébelin and H. Guillet de Chatellus, "Agile photonic fractional Fourier transformation of optical and RF signals," Optica **4**(8), 907–910 (2017).
13. H. Guillet de Chatellus, L. Romero-Cortés, C. Schnébelin, M. Burla, and J. Azaña, "Reconfigurable photonic generation of broadband chirped waveforms using a single CW laser and low-frequency electronics," Nat. Commun. **9**(1), 2438 (2018).
14. C. Schnébelin and H. Guillet de Chatellus, "Reconfigurable photonic arbitrary waveform generation based on a single CW laser and low frequency electronics," in *2018 International Topical Meeting on Microwave Photonics (MWP)*, Toulouse, 2018, pp. 1–3.
15. H. Yang, M. Brunel, H. Zhang, M. Vallet, C. Zhao, and S. Yang, "RF up-conversion and waveform generation using a frequency-shifting amplifying fiber loop, application to Doppler velocimetry," IEEE Photonics J. **9**(6), 1–9 (2017).
16. J. Clement, C. Schnébelin, H. Guillet de Chatellus, and C. R. Fernández-Pousa, "Laser ranging using coherent pulse compression with frequency shifting loops," Opt. Express **27**(9), 12000–12010 (2019).
17. C. Schnébelin, J. Azaña, and H. Guillet de Chatellus, "Programmable broadband optical field spectral shaping with megahertz resolution using a simple frequency shifting loop," Nat. Commun. **10**(1), 4654 (2019).
18. V. Billault, V. Crozatier, G. Baili, G. Feugnet, M. Schwarz, P. Nouchi, D. Dolfi, and H. Guillet de Chatellus, "Regenerative Talbot laser for generating tunable pulse train with a low phase noise," IEEE Photonics Technol. Lett. **31**(22), 1842–1845 (2019).
19. V. Durán, H. Guillet de Chatellus, C. Schnébelin, K. Nithyanandan, L. Djevarhidjian, J. Clement, and C. R. Fernández-Pousa, "Optical frequency combs generated by acousto-optic frequency-shifting loops," IEEE Photonics Technol. Lett. **31**(23), 1878–1881 (2019).
20. K. Patorski, "The self-imaging phenomenon and its applications," Prog. Opt. **27**, 1–108 (1989).
21. J. Wen, Y. Zhang, and M. Xiao, "The Talbot effect: recent advances in classical optics, nonlinear optics, and quantum optics," Adv. Opt. Photonics **5**(1), 83–130 (2013).
22. M. V. Berry and S. Klein, "Integer, fractional and fractal Talbot effects," J. Mod. Opt. **43**(10), 2139–2164 (1996).
23. J. Azaña and M. A. Muriel, "Temporal self-imaging effects: theory and application for multiplying pulse repetition rates," IEEE J. Sel. Top. Quantum Electron. **7**(4), 728–744 (2001).
24. H. Guillet de Chatellus, E. Lacot, O. Hugon, O. Jacquin, N. Khebbache, and J. Azaña, "Phases of Talbot patterns in angular self-imaging," J. Opt. Soc. Am. A **32**(6), 1132–1139 (2015).

Optics EXPRESS

25. G. H. Smith, D. Novak, and Z. Ahmed, "Overcoming chromatic-dispersion effects in fiber-wireless systems incorporating external modulators," IEEE Trans. Microwave Theory Tech. **45**(8), 1410–1415 (1997).
26. C. R. Fernández-Pousa, "On the structure of quadratic Gauss sums in the Talbot effect," J. Opt. Soc. Am. A **34**(5), 732–742 (2017).
27. A. W. Lohman, "An array illuminator based on the Talbot effect," Optik **29**(29), 4337–4340 (1990).
28. C. R. Fernández-Pousa, R. Maram, and J. Azaña, "CW-to-pulse conversion using temporal Talbot array illuminators," Opt. Lett. **42**(13), 2427–2430 (2017).
29. L. Romero-Cortés, M. Seghilani, R. Maram, and J. Azaña, "Full-field broadband invisibility through reversible wave frequency-spectrum control," Optica **5**(7), 779–786 (2018).
30. L. Romero-Cortés, R. Maram, H. Guillet de Chatellus, and J. Azaña, "Arbitrary energy-preserving control of optical pulse trains and frequency combs through generalized Talbot effects," Laser Photonics Rev. **13**(12), 1900176 (2019).
31. S. Matsutani and Y. Ônishi, "Wave-particle complementarity and reciprocity of Gauss sums on Talbot effects," Found. Phys. Lett. **16**(4), 325–341 (2003).
32. H. C. Rosu, J. P. Treviño, H. Cabrera, and J. S. Murguía, "Talbot effect for dispersion in linear optical fibers and a wavelet approach," Int. J. Mod. Phys. B **20**(11n13), 1860–1876 (2006).
33. L. Romero-Cortés, H. Guillet de Chatellus, and J. Azaña, "On the generality of the Talbot condition for inducing self imaging effects on periodic objects," Opt. Lett. **41**(2), 340–343 (2016).
34. P. Kildal, "Asymptotic approximations of radiation integrals: endpoint and double endpoint diffraction," Radio Sci. **19**(3), 805–811 (1984).
35. C. M. Bender and S. A. Orszag, *Advanced Mathematical Methods for Scientists and Engineers: Asymptotic Methods and Perturbation Theory* (Springer, 2013), Chap. 6.
36. R. G. Kouyoumjian and P. H. Pathak, "A uniform geometrical theory of diffraction for an edge in a perfectly conducting surface," Proc. IEEE **62**(11), 1448–1461 (1974).
37. M. Born and E. Wolf, *Principles of Optics* (Elsevier, 2013), Chap. 8.
38. A. B. Carlson, *Communication Systems* (Tata McGraw-Hill Education, 2010), Chap. 5.
39. R. A. Silverman, *Introductory Complex Analysis* (Dover, 1972), Chap. 14.
40. N. Bleistein, "Uniform asymptotic expansions of integrals with stationary point near algebraic singularity," Commun. Pure Appl. Math. **19**(4), 353–370 (1966).
41. L. B. Felsen and N. Marcuvitz, *Radiation and Scattering of Waves* (John Wiley & Sons, 1994), Sect. 4.6a.